Patterns of conserved gp120 epitope presentation on attached HIV-1 virions

Meron Mengistu[a], Ai-hui Tang[b], James S. Foulke Jr.[a], Thomas A. Blanpied[b], Mileidy W. Gonzalez[c], John L. Spouge[c], Robert C. Gallo[a,1], George K. Lewis[a], and Anthony L. DeVico[a,1]

[a]Institute of Human Virology, University of Maryland School of Medicine, Baltimore, MD 21201; [b]Department of Physiology, University of Maryland School of Medicine, Baltimore, MD 21201; and [c]National Center for Biotechnology Information, National Library of Medicine, National Institutes of Health, Bethesda, MD 20894

Contributed by Robert C. Gallo, September 27, 2017 (sent for review March 28, 2017; reviewed by James Arthos, Frank Denaro, and Thomas J. Hope)

A complete picture of HIV antigenicity during early replication is needed to elucidate the full range of options for controlling infection. Such information is frequently gained through analyses of isolated viral envelope antigens, host CD4 receptors, and cognate antibodies. However, direct examination of viral particles and virus–cell interactions is now possible via advanced microscopy techniques and reagents. Using such methods, we recently determined that CD4-induced (CD4i) transition state epitopes in the HIV surface antigen, gp120, while not exposed on free particles, rapidly become immunoreactive upon virus–cell binding. Here, we use 3D direct stochastic optical reconstruction microscopy (dSTORM) to show that certain CD4i epitopes specific to transition state structures are exposed across the surface of cell-bound virions, thus explaining their immunoreactivity. Moreover, such structures and their marker epitopes are dispersed to regions of virions distal to CD4 contact. We further show that the appearance and positioning of distal CD4i exposures is partially dependent on Gag maturation and intact matrix–gp41 interactions within the virion. Collectively, these observations provide a unique perspective of HIV during early replication. These features may define unique insights for understanding how humoral responses target virions and for developing related antiviral countermeasures.

HIV antigenicity | cell attachment | epitope positions | transition state conformation | virion structure

The HIV envelope presents a highly malleable structure to the immune system. This characteristic has frustrated efforts to efficiently use antibodies as weapons against HIV infection. On free virions, the HIV envelope is a trimer (composed of two antigens, gp120 and gp41) that presents a variety of broadly neutralizing epitopes. However, the genetic mutability of the HIV genome gives the virus an extensive capacity to escape recognition by all known neutralizing antibodies (1). The most immutable and indispensable epitopes extant within the envelope trimer arise on a changing array of transition state structures formed during attachment and entry. The process begins when the gp120 component attaches to a CD4 receptor and then to a coreceptor (CCR5 or CXCR4) on target cells (2, 3). CD4 attachment causes conformational rearrangements in the gp120 trimer, resulting in a transition state structure (4) that presents the coreceptor binding site as well as other CD4-induced (CD4i) epitopes on gp120 (5). CD4i and related transition state gp120 epitopes are highly conserved across viral variants and comprise signatures for transmitted/founder HIV variants (6).

In theory, the conserved nature and essential replicative functions of transition state domains offers a venue to guide humoral immunity toward the broadest possible reactivity (1) against diverse HIV strains. This possibility remains under investigation. Most antibodies against transition state epitopes are poorly neutralizing or nonneutralizing in conventional in vitro assays, which measure chemical inactivation of virions (e.g., receptor blocking or interference in other envelope functions). These findings, along with crystal structures and cryo-EM image of soluble envelope glycoproteins and/or free virions (7–13), have been taken as evidence that transition state structures emerge only at target cell–HIV contact zones, where they are occluded and nonimmunoreactive (10–18). However, other lines of in vivo and in vitro evidence suggest that attachment-driven, immunoreactive epitope exposure does occur in the envelope structure under various conditions. Certain anti-envelope monoclonal antibodies (mAbs) neutralize HIV via epitopes formed post attachment structures (19). Furthermore, antibodies recognizing a range of conserved transition state gp120 domains, including CD4i epitopes, mediate Fc receptor (FcR)-dependent humoral effector functions [e.g., antibody-dependent cellular cytotoxic (ADCC)] against cell-bound virions (20) and cells supporting the spread of infection (21). Such activities have been associated with reduced infection risk in the RV144 clinical trial (22–24), in nonhuman primate tests of HIV vaccine candidates (25, 26), and in natural HIV transmission (27, 28). Confocal microscopy studies demonstrated that CD4i epitope exposure can spread and persist on surface membranes engaged in HIV-driven cell–cell fusion (29). In accordance, Ig domain-based agents targeting a CD4i epitope were shown to suppress HIV infection in ex vivo cultures (30, 31).

Significance

A complete picture of HIV antigenicity during early replication is needed to elucidate the full range of options for controlling infection through humoral immunity. The HIV envelope protein, gp120, experiences key structural rearrangements during host cell attachment, leading to exposure of highly conserved epitopes on the virion surface. These epitopes enable Fc-mediated antiviral effector functions that may be relevant to HIV prevention. Here, we used 3D superresolution microscopy to show how gp120 epitopes are rapidly exposed distal to cell–virus interfaces, introducing the opportunity for unconstrained antibody binding. These previously unrecognized facets of HIV antigenicity further define relationships between retroviral infection and immunity and should facilitate the development of antibody-based approaches for HIV prevention.

Author contributions: M.M. and A.L.D. designed research; M.M. and J.S.F. performed research; M.M., A.-h.T., and T.A.B. contributed new reagents/analytic tools; M.M., A.-h.T., J.S.F., T.A.B., and A.L.D. analyzed data; M.W.G. and J.L.S. provided statistical analyses; R.C.G. provided instrumentation, guidance, and support; G.K.L. and A.L.D. supervised experiments; and M.M., M.W.G., J.L.S., R.C.G., G.K.L., and A.L.D. wrote the paper.

Reviewers: J.A., National Institutes of Health; F.D., Morgan State University; and T.J.H., Northwestern University.

The authors declare no conflict of interest.

Data deposition: The sequences reported in this paper have been deposited in the GenBank database (accession nos. KM555100 and KM555101), and the custom code reported in this paper has been deposited in MATLAB File Exchange (title: HIV Sphere Fit and Angle Calculation; file ID 57198).

[1]To whom correspondence may be addressed. Email: rgallo@ihv.umaryland.edu or adevico@ihv.umaryland.edu.

This article contains supporting information online at www.pnas.org/lookup/suppl/doi:10.1073/pnas.1705074114/-/DCSupplemental.

A better understanding of epitope exposure on individual virions attached to host cells would contribute greatly to understanding whether and how humoral responses recognize transition state domains.

This information may be derived from direct visualization of cell-bound particles at the single-molecule level.

In this context, it is important to consider that the epitope exposures most relevant to anti-HIV immunity occur on mature, replication-competent virions. It has been repeatedly shown that the overall structure and function of the HIV trimer is determined by integrated structural networks and connections formed by the gp41 C terminus and the mature viral matrix protein, p17 (32–40). gp41–matrix interactions may involve direct protein–protein binding (37, 41, 42) and/or other steric relationships within the viral membrane (37). Consequently, the distribution of trimeric envelope spikes (40) and the presentation of their epitopes (36) differ significantly on mature vs. immature virions. Characteristics similar to those of immature virions can be produced by truncations of the gp41 C terminus that disrupt matrix interactions (36, 40).

Recently, we used confocal microscopy to delimit the antigenic characteristics of HIV virions during the course of attachment and entry (43). These studies showed that target cell binding causes HIV virions to present, for various periods of time, an array of immunoreactive transition state gp120 epitopes that are otherwise hidden on free virions. Importantly, epitope exposure patterns were influenced by hallmarks of active replication including coreceptor expression and membrane fusion capacity. Here, we employ 3D superresolution imaging to examine the exposure of transition state epitopes on single, cell-bound viral particles under conditions that allow or restrict maturation and/or natural gp41–matrix interactions. We show that the attachment process triggers the exposure of immunoreactive CD4i epitopes across a virion surface, extending away from primary CD4 contact zones. We further show that this process relies on maturation-dependent structural aspects of the virion.

Results

Imaging gp120 Epitope Exposure on Cell-Bound HIV Virions. Previously (43), we developed a system for high-resolution imaging of the HIV attachment process based on fluorescence-labeled, entry-competent HIV_{JRFL} pseudovirions [representing a CCR5-tropic, neutralization-resistant "tier 2" strain (44)] and TZM-bl target cells. Briefly, cell–virus mixtures are cocultured and fixed at specified time points; cell-bound virions are detected via their fluorescence signals; and epitope exposure is interrogated with directly conjugated anti-gp120 mAbs (*Methods*). This system revealed that host cell attachment causes CD4i epitope immunoreactivity on bound virions. Such epitope exposures were not associated with shed gp120 or other aberrant forms of antigen but were linked to parameters that mark active virus–cell fusion and entry processes.

Given this framework, we refined and adapted the imaging approach toward 3D direct stochastic optical reconstruction microscopy (dSTORM) superresolution imaging of cell-bound HIV particles. A 30-min virus–cell interaction time was selected before fixation to provide robust gp120 epitope signals (43). Virion contents were marked by Alexa 360-conjugated CLIP–Vpr; virion membranes marked by Alexa 546-conjugated SNAP–ICAM-1 (incorporated during budding); proximal cell surface CD4 marked by Alexa 647-conjugated anti-CD4 mAb OKT4; and gp120 epitopes marked by Alexa 488-conjugated test mAbs.

Potential regions of interest (ROIs) containing putative bound virions were first identified using total internal reflection fluorescence (TIRF) signals from CLIP–Vpr. Such ROIs were then surveyed for Gaussian dSTORM signals (described in *Methods*). ROIs were selected for advanced analyses only in cases where Alexa 546-conjugated SNAP–ICAM-1 and Alexa 360-conjugated CLIP–Vpr signals were coincident within a 200-nm-diameter boundary, which in turn was located proximal (see below) to a cell surface CD4 signal (indicated by Alexa 647-conjugated mAb OKT4). Selected ROIs were surveyed for gp120 epitope exposures using Alexa 488-conjugated test mAbs.

Example images showing two ROIs selected in this manner are shown in Fig. 1*A*, *Left*. Overlays of Gaussian fluorescence images are shown in Fig. 1*A*, *Right*, where cell surface CD4 is stained red and SNAP–ICAM-1, blue. Gp120 is stained green with the anti-CD4i mAb A32, which was previously shown to be reactive with bound virions (43). Translation of the signals to 3D dSTORM images is shown in Fig. 1*B*, marked with the corresponding numerical designations.

Taking advantage of the 3D SNAP–ICAM-1 and test mAb localization signals (Fig. 1*B*), we developed a computational algorithm (enabled by a custom MATLAB code; *SI Methods*) that delimits the periphery of a virion sphere, oriented relative to a target cell surface presenting CD4 receptors. Fig. 1*C* shows representative depictions derived from the algorithm as applied to signals shown in Fig. 1*B*. The algorithm marks the relative positions of CD4, gp120 epitope, and SNAP–ICAM-1 signals on any given rendering (Fig. 1*C*, using same color-scoring scheme as in Fig. 1*B*). Processed in this manner, pooled renderings of wild-type (WT) virion ROIs from all experiments (see below; 455 ROIs total) reflected a mean particle diameter of 180.72 ± 27.95 nm (mean ± SD; Fig. S1*A*: WT). Such measures conform to the selection criteria used here and also agree with previously determined HIV virion sizes (12, 13, 45).

The anti-CD4 mAb OKT4 signals were used for establishing the spatial orientations of epitope exposures on the predicted virion sphere. Specifically, CD4 signals positioned within 50 nm

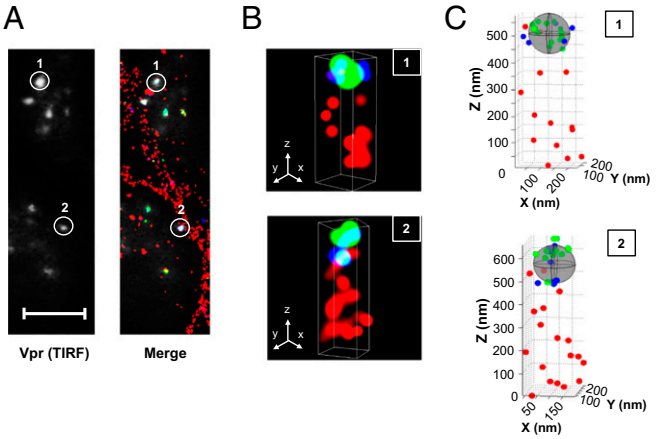

Fig. 1. Development of 3D dSTORM images representing cell-bound HIV virions. Particles were allowed to interact with TZM-bl cells and imaged as described in *Methods*. (*A*, *Left*) Two representative TIRF images of Vpr signals used to select ROIs (circled). (Scale bar, 5 μm.) (*A*, *Right*) Merged dSTORM Gaussian signals for Alexa Fluor 546-labeled SNAP–ICAM-1 (blue); Alexa Fluor 488-labeled mAb A32 (green); and Alexa Fluor 647-labeled anti-CD4 antibody OKT4 (red) overlapped with TIRF Vpr images. (*B*) Translation of signals from the two ROIs in *A* to 3D dSTORM images. The "Z" arrow is pointing upward away from the target cell. (*C*) The 3D positional coordinates of dSTORM localizations for mAb A32 and SNAP–ICAM-1 in each of the ROIs were utilized to render a spherical virion (shown in gray) using a custom MATLAB code as described in *Methods* and *Supporting Information*. The anti-CD4 mAb, SNAP–ICAM-1, or mAb A32 fluorescence signals were used to fit centroids that mark CD4 (red dots), ICAM-1 (blue dots), and gp120 epitope (green dots) positions, respectively. The dot sizes are arbitrary and are not intended to depict the relative localization precision of each dye. Relative distances in three dimensions are shown in nanometers.

of the rendered virion surface were taken as the most likely contact points for receptor-mediated target cell attachment. Multiple images were generated in this manner for all anti-HIV envelope mAbs in the test panel, which included mAb 2G12, a constitutively exposed neutralizing gp120 epitope; and anti-CD4i mAbs A32, C11, and 17b, as well as for mutant viruses (see below).

gp120 Immunoreactivity Patterns on TZM-bl Cell-Bound HIV Virions. We first compared the immunoreactivity of the anti-gp120 mAbs with cell-bound HIV virions by recording the number of localized events for at least 100 ROIs per epitope/antibody, selected as described in Fig. 1. There were no significant differences in the mean number of localizations (8–10) between the mAbs regardless of specificity, in accordance with our previous findings (43) (Fig. 2*A*). Each mAb binding experiment included comparative negative controls in which Synagis was tested under matched binding conditions. No more than one Synagis localization signal was recorded in Vpr-positive, SNAP–ICAM-1-positive ROIs in any experiment. ROIs with four to eight localized events were most frequently detected with anti-gp120 mAbs (Fig. 2*B*) regardless of antibody/epitope. Under the conditions used, all antibodies showed similar signal distributions [Wilcoxon–Mann–Whitney *U* test; $P > 0.05$; false-discovery rate (FDR) threshold of $q < 0.05$] among the ROIs surveyed.

gp120 Epitope Exposure Relative to Potential CD4 Contacts. Three-dimensional dSTORM imaging and refinements (shown in Fig. 1) were used to examine epitope distribution patterns relative to potential CD4–virion contact zones. Virions bound to entry-permissive cells experience variable numbers of potential CD4 contacts due to convolutions in the target cell surface. To mark multiple contacts, the calculated density sphere of each particle was divided into geometric octants. Any octant positioned within 50 nm of an anti-CD4 signal was labeled as a potential contact zone [based on the ∼50-nm axial resolution of N-STORM (46)]. Examples of three image scenarios where one, two, or three octants are potential CD4 contact zones (marked with a blue "x") are shown in Fig. 3*A*. The numbers of CD4 contact zones (hereafter called CD4 contact octants) as distributed within the bound virion population are shown in Fig. S1*B*.

The initial method used to localize gp120 epitope exposure was to color score the octants according to their orientations and distances from likely CD4 contact points. The antibody signals detected in each color category could then be quantified and localized to provide a broad landscape of epitope exposure. Color assignments were as follows: an assigned CD4 contact, yellow; an octant sharing sides with the CD4 contact octant, green; within an octant with tips meeting the CD4 contact octant, cyan; within octants not engaging the CD4 contact octant, pink. Instances where three or more octants were designated as potential CD4 contact zones (Fig. 3*B*, *Bottom*) placed most or all antibody reactivity in the CD4 contact octant or an adjacent octant. In comparison, cases where there were one to two CD4 contact octants (Fig. 3*B*, *Top*) afforded a better capacity to determine how far from CD4 contact an epitope might be exposed. Accordingly, our analyses comprised not only the entire bound virion population but also the subset of ROIs (roughly 45% of the total bound virions across all experiments; Fig. S1*B*) with one to two CD4 contact octants. At least one-third of the total ROIs surveyed in each antibody-staining experiment (Fig. 4*A*) reflected one to two CD4 contacts; the majority of them were reactive with the test mAb (Fig. 4*B*).

The mAb 2G12 recognizes a constitutively expressed neutralizing epitope and has previously been used as a marker for envelope distribution on HIV virions (40). On virions attached to poly-L-lysine–coated coverglass, 2G12 signals were usually detected in one to four octants and most frequently in two octants (Fig. S1*C*, dark red). In comparison, 2G12 epitope exposures were dispersed across more octants within the overall cell-bound virion population (labeled "ALL"; P = 1.71e-04; χ^2 test) (Fig. S1*C*, bright red). Greater dispersal was also observed in the subset of these virions with one to two CD4 contact octants (labeled "1 or 2"; $P = 0.008$; χ^2 test) (Fig. S1*C*, orange). Alternatively, SNAP–ICAM-1 distribution also differed between free and cell-bound virions. In this case (Fig. S1*D*), the entire population of cell-bound virions exhibited signals skewed toward a narrower range of immunoreactive octants compared with free particles on coverglass [$P = 0.008$ (vs. all contacts) and $P = 2.71$e-04 (vs. 1 or 2 contacts); χ^2 test]. Thus, virion–cell attachment appeared to alter the distributions of both envelope and SNAP–ICAM-1, but not in a coordinated manner.

In ROIs with one to two CD4 contact octants, mAb 2G12 staining occurred in the same (yellow), or adjacent virion octants (green or blue) (Fig. 4*C*). Staining most frequently occurred in the "green" octants, which represent the greatest overall surface area in the ROI subset. Notably, the distribution of anti-CD4i mAb signals (A32, C11, and 17b) matched those of mAb 2G12, appearing outside the predicted CD4 contact zones. Overall, there were no significant differences between the signal distributions of CD4i mAbs vs. mAb 2G12 (P = 0.903, 0.985, and 0.393; multiway Fisher), respectively (Fig. 4*C*).

In a similar manner, CD4i epitope exposures observed in the entire bound virion population (Fig. S2*A*) frequently occurred in the green octants regardless of epitope. Compared with the subset with one or two CD4 contacts, more ROIs exhibited signals in the CD4 contact ("yellow") octants (Fig. S2*B* vs. Fig. 4*C*). This difference most likely stems from the inclusion of ROIs with three or more potential CD4 contact octants, where "crowding" of CD4 molecules on the virion surface increases the chances of proximity to an envelope spike presenting a gp120 epitope.

To refine these observations, we applied a complementary method ("angle analysis") to quantify angular relationships between CD4 and gp120 epitope positions on bound virion surfaces (*Methods* and *Supporting Information*). Each epitope exposure within an ROI is traced to the nearest CD4 located ≤50 nm thick from the calculated virion periphery. Rays from the anti-gp120 mAb localization signal and the nearest anti-CD4 mAb (OKT4) signal are then extended to vertices positioned at the centers of virion spheres (shown schematically in Fig. 3*C*). The angle between rays (designated mAb–CD4 signal angle) then reflect the distance between the two signals along an arc across the spherical surface. It must be noted that octants can contain

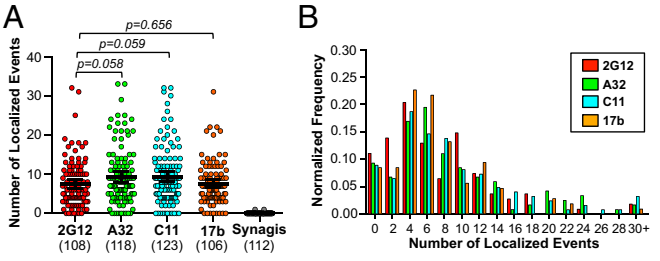

Fig. 2. mAb binding signals in ROIs containing cell-bound virions. HIV particles were allowed to interact with TZM-bl cells as described in *Methods*. (*A*) Scatter plots of localized events from labeled anti-gp120 or control antibodies in superresolution ROIs selected as described in *Methods*. The numbers of ROIs examined for each test condition are shown in parentheses. Black lines indicate the mean and SEs. The *P* values (Wilcoxon–Mann–Whitney *U* test) for these comparisons are indicated at *Top*. (*B*) Histogram plots of the signal data shown in *A*. Each experiment was conducted under identical incubation conditions using the same preparation of labeled virus. Similar results were obtained in experiments using a separate preparation of virus.

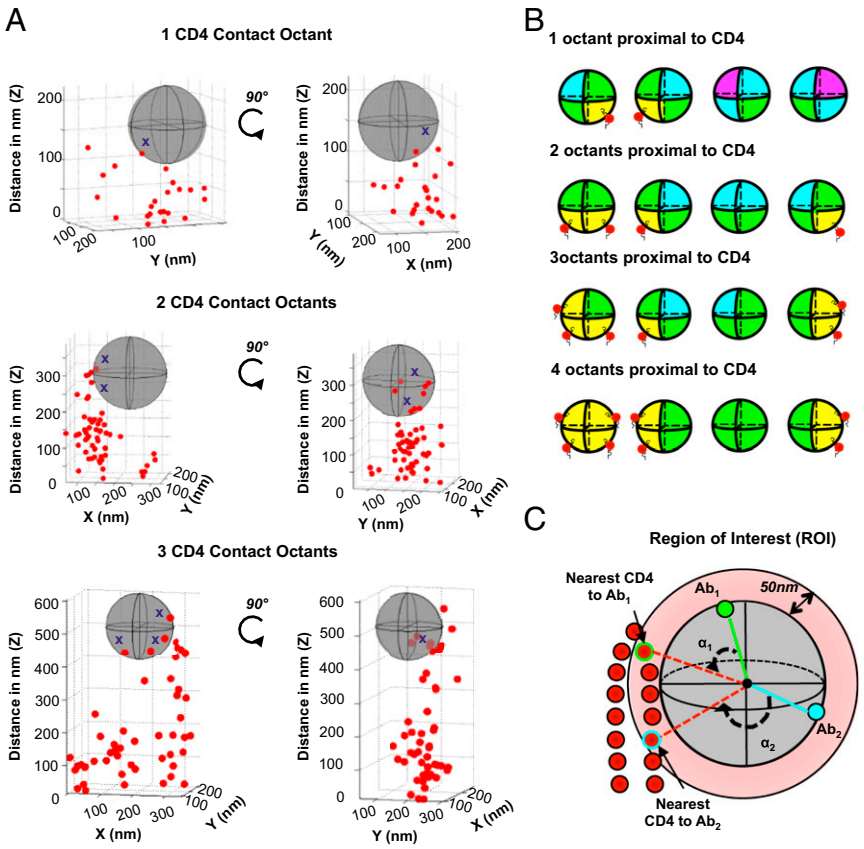

Fig. 3. Methods for positioning gp120 epitopes relative to cell surface CD4. The 3D dSTORM images were obtained processed as shown in Fig. 1 and described in *Methods*. (*A*) Example MATLAB-processed images of three HIV–target cell contact scenarios. The mAb OKT4 signals positioned ≤50 nm of the virion spheres are taken as CD4 receptors in potential contact with the virion (marked with blue crosses). Note that, in the renderings, the axis scalings increase from *Top* to *Bottom* to reflect a wider perspective of how multiple CD4 receptors surround the virion. However, in all cases, the virion spheres are of equivalent sizes. (*B*) Schematic depictions of octant color scoring according to proximity with a potential CD4 contact zone (yellow). Octants sharing sides with the CD4 contact octant are green; octants with tips meeting the CD4 contact octant, cyan; octants not engaging the CD4 contact octant, pink. Each color was assigned a number to facilitate statistical comparisons: yellow, 1; green, 2; cyan, 3; pink, 4. Also shown are coloring scenarios where one to four potential CD4 contacts occur, as designated. From *Left* to *Right* are four successive 90° rotation views of the stylized virion sphere. (*C*) Schematic representation of how the angle analysis method is used to position gp120 epitope exposures relative to the nearest CD4 receptor contact. The illustration exemplifies an operation where the SNAP–ICAM-1 and anti-gp120 mAb localization coordinates are used to fit spheres (gray) circumscribing HIV particle volumes, using a custom MATLAB code (as in Fig. 1 and *Methods*). Anti-CD4 (mAb OKT4), SNAP–ICAM-1, or anti-gp120 (test mAb) fluorescence signals are used to fit centroids marking the positions of CD4, SNAP–ICAM-1, or gp120 epitopes, respectively. Two stained gp120 epitopes are marked in the illustration as green and blue dots (Ab1 and Ab2). CD4 positions are shown as red dots. Any CD4 position within a 50-nm-wide orbit (pink halo) of the predicted virion surface is taken as a potential virus–receptor contact. Spherical angles between the calculated positions of each epitope and its nearest putative CD4 contact (red dots with colored borders within the pink halo) are determined, using the center of the virion sphere as the vertex for the corresponding rays (*Methods*). Accordingly, two epitope–CD4 signal angles (α1 and α2 for Ab1 and Ab2, respectively) are derived from the localization data.

multiple CD4 and/or gp120 molecular signals. Thus, multiple angles can be extracted from a single ROI.

A comparison of ROI subsets revealed differences in the distribution of mAb 2G12–CD4 signal angles according to whether there were one to two vs. three or more CD4 contact octants (Fig. S1*E*). Both frequency histogram and cumulative frequency plots showed that ROIs with one to two CD4 contact octants had generally larger mAb 2G12–CD4 signal angles compared with ROIs with three or more CD4 contact octants (P = 1.36e-05; Wilcoxon–Mann–Whitney U test). As noted above, smaller mAb–CD4 signal angles could be expected when CD4 molecular contacts are "crowded" onto the virion surface, reducing the possible distance to an envelope spike.

Cell-bound virions were also recognized by a neutralizing CD4–Ig fusion protein (sCD4–Ig; conjugated to Alexa 488) (47), targeted to the constitutively expressed receptor binding domain on free gp120 (Fig. S1*F*). Such reactivity most likely involved envelope spikes on the virion oriented away from the immediate cell contact zone. However, sCD4–Ig–CD4 receptor signal angles were significantly skewed (P = 5.46e-06; Wilcoxon–Mann–Whitney U test) toward larger values (i.e., greater distances from the cell surface) vs. what was measured for mAb 2G12. The sCD4–Ig pattern indicates that the CD4 binding sites of envelope trimers may be distinctly perturbed within areas of the virion closest to cell surface contact, in a manner that impedes reactivity with sCD4–Ig but preserves binding to mAb 2G12.

Application of the angle analysis approach to other gp120 epitopes showed that the histogram and frequency distributions of mAb 17b–CD4 signal angles were not significantly different from those of mAb 2G12 (P = 0.556; Wilcoxon–Mann–Whitney U test) in the subpopulation with one to two CD4 contact octants (Fig. 4*D*, which includes the mAb 2G12 binding localizations described above for comparison). The mAb A32–CD4 angles showed a trend toward larger values compared with mAb 2G12–CD4 angles (P = 0.038; Wilcoxon–Mann–Whitney U test) but did not survive the multiplicity correction (Table S1). In comparison, the mAb C11–CD4 signal angles were significantly larger than what was

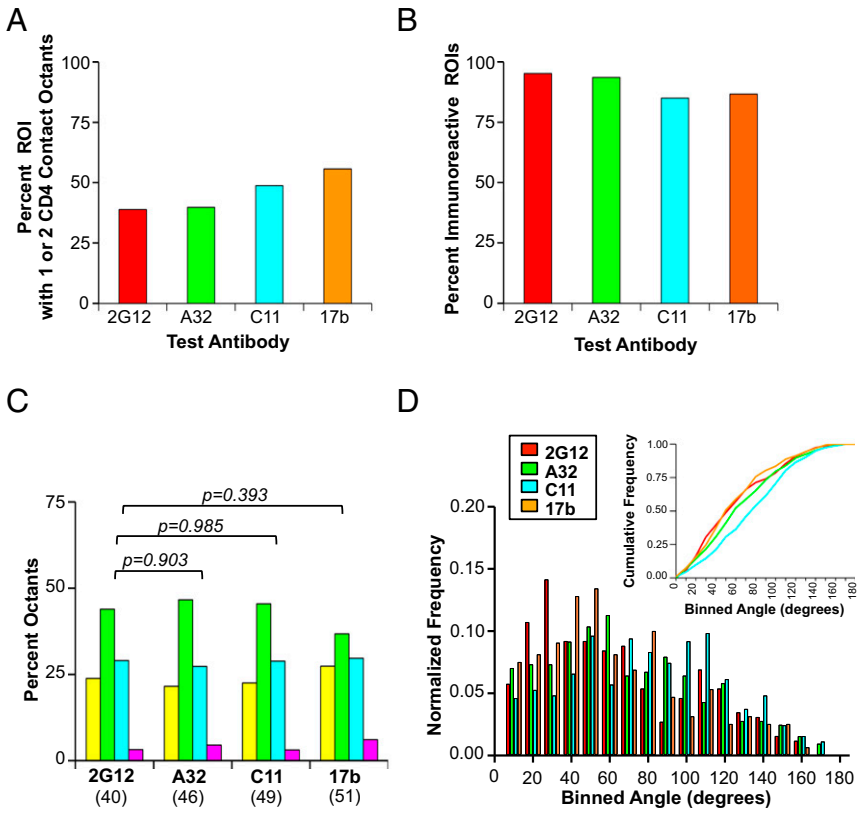

Fig. 4. The gp120 epitope localization relative to cell surface CD4 on WT HIV virions. (*A*) Fractions of all surveyed ROIs (totals shown in Fig. 2*A*) reflecting one or two potential virion contacts with CD4 under each antibody test condition. (*B*) Fraction of the one to two potential CD4 contact ROIs shown in *A* exhibiting reactivity with the indicated test antibody. The anti-gp120 immunoreactive ROIs were used for epitope location analyses shown in the following panels: (*C*) octant color scoring of 2G12, A32, C11, or 17b epitope exposures as described in Fig. 3*B*. The numbers of ROIs examined are shown in parentheses. The *P* values for pairwise comparisons are shown at *Top* (multiway Fisher test). (*D*) Angles between CD4 contact-test mAb signals (for ROIs shown in *C*) were determined as shown in Fig. 3*C* (*Methods*). The frequency distributions of calculated angles for each antibody/epitope are shown in histogram plots; *Insets* show the cumulative frequency plots of the same datasets with corresponding color designations. Similar results were obtained in experiments using a separate preparation of virus.

observed with any other antibody ($P = 1.10e-07$; Wilcoxon–Mann–Whitney *U* test).

The mAb–CD4 signal angles for bound virion populations having three or more CD4 contact octants were significantly skewed toward smaller values (Table S1) compared with the ROI subset with one to two contact octants (mAb 2G12, $P = 1.36e-05$; mAb A32, $P = 5.28e-07$; mAb C11, $P = 2.20e-07$; mAb 17b, $P = 0.020$). This trend was also seen with SNAP–ICAM-1 distribution ($P = 7.06e-14$).

Findings that the entire bound virion population reflected a greater fraction epitope exposures in octants containing potential CD4 contacts (compared with the subset with one to two contacts) is explained by the inclusion of the three or more CD4 contact virions, which contain smaller mAb–CD4 distances.

Envelope–Matrix Interactions Partially Determine CD4i Epitope Exposure. The processing of HIV gag during maturation results in interactions between matrix proteins and the gp41 C terminus that have significant impact on the disposition of the HIV envelope trimer (32–35). We generated two variants of the HIV_{JRFL} pseudovirus to explore the impact of maturation on CD4i epitope exposures. The first contained a matrix/capsid processing site mutation (Y132I) that blocks proteolytic processing of the Gag precursor, resulting in the formation of aberrant cores and noninfectious virions (48). The second contained a mutation (ΔCT) causing truncation of the gp41 C terminus at residue 708, thus preventing gp41 interactions with the matrix (49). Similar to WT virions, these mutants incorporated SNAP–ICAM-1 and CLIP–Vpr for visualization. The Y132I and ΔCT virions expressed equivalent amounts of gp120:p24 ratio compared with WT (*SI Methods*). The calculated mean diameters (Fig. S1*A*) for mutant virions were slightly smaller than WT HIV particles (173.76 ± 30.47 nm for Y1232I mutants, $P = 0.011$; and 164.17 ± 33.07 nm for ΔCT mutants; $P = 1.16e-08$, Wilcoxon–Mann–Whitney *U* test).

Each mutant virus was fluorescence-labeled and cocultured with target TZM-bl cells for 30 min at 37 °C. The mutations did not appreciably impact the degrees of CD4 engagement vs. WT virions. For example, the fractions of ROIs containing virions with one to two CD4 contact octants did not vary more than twofold among variants or test conditions (Fig. 5*A*). A comparison of overall bound virion populations revealed that the mutations did not alter the presentation of the 2G12 epitope among ROIs. The numbers of mutant ROIs presenting the 17b epitope was reduced vs. the WT virus population, but only to a minor degree. In comparison, the mutations clearly reduced the numbers of ROIs presenting any A32 or C11 mAb signal vs. WT (Fig. S3*A*). Furthermore, the magnitude of such differences depended on the numbers of CD4 contacts within the ROI. Comparisons of ROI subsets partitioned according to three or more CD4 contact octants (Fig. S3*B*) showed less impact of the mutations in reducing the numbers of ROIs expressing the epitopes. However, similar comparisons of ROIs partitioned based on one to two CD4 contact octants (Fig. 5*B*) revealed greatly reduced numbers

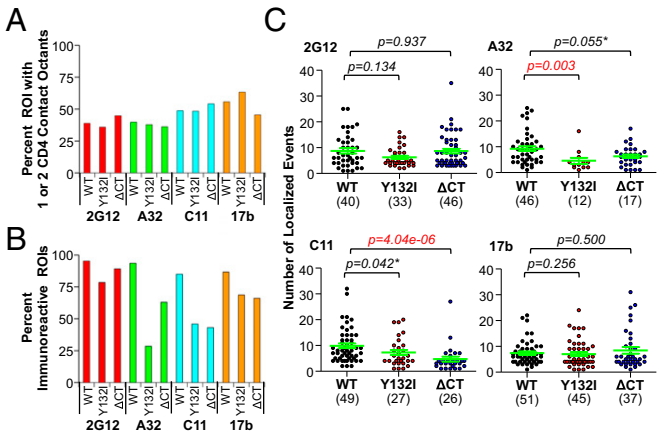

Fig. 5. Comparison of gp120 epitope exposures on WT and mutant virions bound to target cells. Virions are designated as WT, immature (Y132I), or gp41-truncated (ΔCT) as mentioned in the text. The total numbers of ROIs surveyed for each experiment (i.e., regardless of CD4 contact numbers) were as follows: mAb 2G12: $n = 108$ (WT), $n = 117$ (Y132I), $n = 125$ (ΔCT); mAb A32: $n = 118$ (WT), $n = 111$ (Y132I), $n = 127$ (ΔCT); mAb C11: $n = 123$ (WT), $n = 130$ (Y132I), $n = 120$ (ΔCT); and mAb 17b: $n = 106$ (WT), $n = 106$ (Y132I), $n = 123$ (ΔCT). (*A*) Fractions of the ROIs for each virus type exhibiting one to two CD4 contact octants are shown. WT data are the same as plotted in Fig. 4*A* and are reproduced here for comparison. (*B*) Fraction of the one to two potential CD4 contact ROIs shown in *A* exhibiting reactivity with the indicated test antibody. The numbers of such ROIs for each experimental condition match the values shown in *C*. (*C*) Scatter plots showing the number of localized events detected in WT or mutant ROIs that exhibited any detectable mAb reactivity. The numbers of such ROIs examined for each condition are shown in parentheses. Green lines indicate the geometric mean (center) and SEs (bars). The *P* values for each pairwise comparison (Wilcoxon–Mann–Whitney *U* test) are indicated on *Top* of panels; *P* values with an asterisk (*) did not survive the multiplicity correction at $q < 0.05$ but are significant at $q < 0.075$.

of mutant ROIs with any discernable A32 or C11 mAb signal compared with WT (data from Fig. 4*B* reshown for comparison). Neither subpopulation reflected significant impact of the mutations on 2G12 epitope exposure. The modest impact of the mutations in reducing ROIs exhibiting mAb 17b binding was not appreciably altered by partitioning according to the amount of CD4 contact.

Given these observations, we examined whether the fractions of mutant ROIs retaining evidence of any CD4i staining signal showed a reduction in the numbers of epitopes exposed. This was determined according to the number of localized fluorescent events emanating from bound cognate mAbs, as previously described (43). In this case, the numbers of localized events are proportional to the numbers of mAbs in the ROI, which is in turn a measure of epitope presentation.

We first examined the ROI subsets with one to two CD4 contact octants, where the mutations had the greatest effects. As shown in Fig. 5*C*, the mutations did not appear to significantly alter the numbers of mAb 2G12 or 17b localized events compared with WT particles (derived from the corresponding subset of values shown in Fig. 2*A*). Within the minor fraction of the Y132I mutant virions exhibiting any evidence of reactivity with mAb A32 (Fig. 5*B*), the numbers of localized events/ROI (Fig. 5*C*) were significantly reduced vs. WT ($P = 0.003$; Wilcoxon–Mann–Whitney *U* test). The mAb C11 localization signals on Y132I mutants also trended lower vs. WT virions ($P = 0.042$; Wilcoxon–Mann–Whitney *U* test), although this difference did not survive multiplicity corrections (Table S1). A reciprocal result was observed (Fig. 5*C*) with the ΔCT mutants. In this case, mAb C11 localization signals were significantly lower vs. WT virions ($P = 4.04e\text{-}06$; Wilcoxon–Mann–Whitney *U* test), while mAb A32 localized events only showed a trend ($P = 0.055$, Wilcoxon–Mann–Whitney *U* test). Such differences between WT and mutant virions were not restricted to the ROI subsets with one to two CD4 contact octants. In the overall bound virion populations, mAbs A32 and C11 localized events were significantly lower on both Y132I and ΔCT mutants. The mAbs 2G12 and 17b localized events were similar in ROIs from all virus variants (Fig. S3*C* and Table S1).

The above measures established that maturation-defective/immature HIV particles have an impaired capacity to express CD4i epitopes. Accordingly, we further examined whether the epitopes that can become exposed under these circumstances exhibit a different spatial relationship with CD4 contacts vs. WT virions. This question was first examined by applying the color-scoring method to the ROI subset with one to two CD4 contact octants, which allows a broad array of distances between CD4 and envelope. As shown in Fig. 6*A*, the positions of 2G12 and 17b epitope exposure relative to CD4 contacts were not significantly different among virus types. However, the A32 and C11 mAb binding signals on Y132I mutant virions tended to be closer to CD4 contacts, falling within (yellow) octants, with greater frequency vs. WT. The difference was particularly prominent for A32, where the increase in contact octant signals on the mutant virus was reciprocal to the decrease in signals in an adjacent octant ($P = 0.012$; multicategory Fisher exact test). To a lesser extent, the ΔCT mutant ROIs also trended toward an increases frequency of A32 and C11 epitope signals in yellow octants with concurrent decreases in green octants.

In the angle analyses, both frequency histogram and cumulative frequency plots (Fig. 6*B*) indicated that the mAb 2G12–CD4 signal angles were moderately but significantly skewed toward larger values on ΔCT mutant vs. WT virions ($P = 0.001$; Wilcoxon–Mann–Whitney *U* test), a difference not apparent in the broader color-scoring method (Fig. 6*A*). A similar trend was seen in the mAb 17b–CD4 signal angles ($P = 0.021$; Wilcoxon–Mann–Whitney *U* test). However, an opposing and more obvious trend (Fig. 6*B*) occurred with mAb A32–CD4 and mAb C11–CD4 angles. In these cases, and consistent with the color-scoring patterns, mAb C11–CD4 signal angles were significantly skewed toward smaller values on Y132I and ΔCT mutant vs. WT viruses ($P = 1.303e\text{-}05$ and $4.783e\text{-}09$, respectively; Wilcoxon–Mann–Whitney *U* test). Similarly, mAb A32–CD4 signal angles were significantly skewed toward smaller values on Y132I and ΔCT mutant vs. WT viruses ($P = 9.49e\text{-}05$ and $6.36e\text{-}07$, respectively; Wilcoxon–Mann–Whitney *U* test).

These trends were also evident in the entire bound virion populations. The mAbs A32 and C11 signals on both mutant virus types were more frequently found in yellow over green octants compared with WT virions (Fig. S4*A* and Table S1) and thus situated more closely to CD4. Both frequency histogram and cumulative frequency plots of angle analyses applied to the entire bound virion populations (Fig. S4*B* and Table S1), indicated significantly smaller mAb A32–CD4 and mAb C11–CD4 angles on mutant vs. WT virions.

Importantly, the epitope distributions described above were peculiar to gp120 and not generalizable to every virus surface antigen. This was revealed by parallel analyses of SNAP–ICAM-1 signals. The SNAP–ICAM-1 localized events measured across all experiments were not significantly different (Fig. S5*A* and Table S1), indicating an equivalent incorporation of the protein among virus variants. Among all ROIs, there seemed to be less SNAP–ICAM-1 in the yellow CD4 contact octants (Fig. S5*B*) on Y132I mutants compared with the other virions ($P = 0.006$; Wilcoxon–Mann–Whitney *U* test) in the color-scoring method. However, such differences were not apparent in the angle analyses (Fig. S5*C*). In the subset of ROIs with one to two CD4 contact octants, the distribution of SNAP–ICAM-1 localized events was not significantly different across virus types (Fig. S5 *E* and *F*).

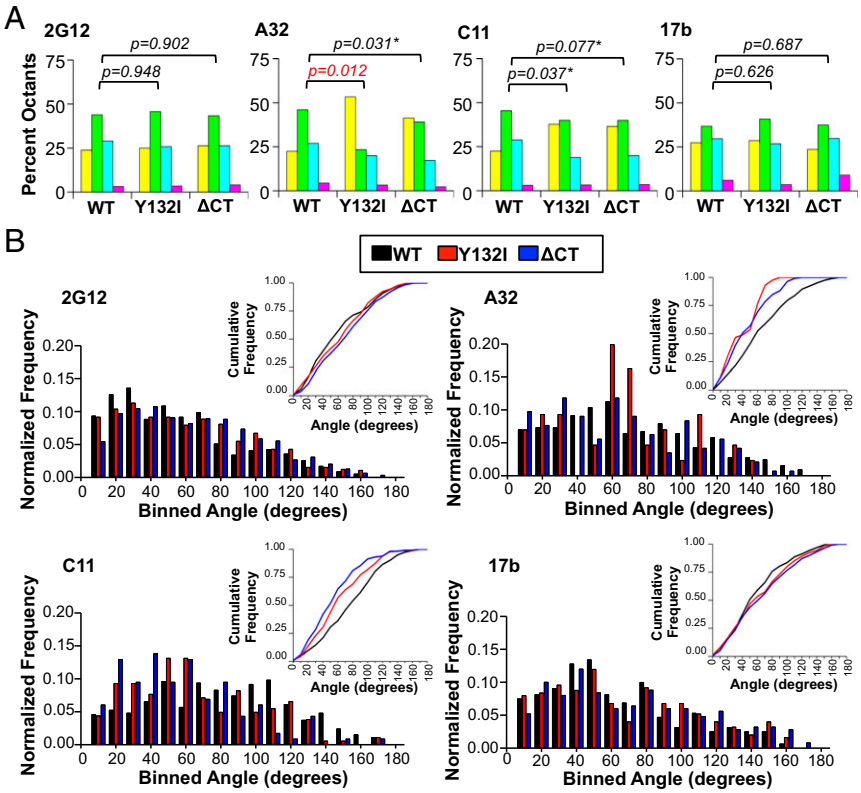

Fig. 6. Analyses of gp120 epitope localizations on the minor fractions of Y132I and ΔCT mutant viruses exhibiting cognate antibody reactivity. ROIs containing mutant viruses from Fig. 5*C* and WT viruses from Fig. 4*A* were analyzed and compared. These datasets represented only the subpopulations of virions with one to two CD4 contact octants. (*A*) Octant color scoring of 2G12, A32, C11, or 17b epitope exposures as described in Fig. 3*B*. The *P* values for each pairwise comparison (multiway Fisher test) are indicated at *Top*; *P* values with an asterisk (*) are trending but did not survive multiplicity correction. (*B*) Angles between CD4 contact-test mAb signals were determined as shown in Fig. 3*C* (*Methods*). The frequency distributions of angles between indicated mAb and nearest CD4 signals are shown in histogram plots for WT (black) HIV particles as well as Y132I (red) and ΔCT mutant (blue) virions. *Insets* show the cumulative frequency plots of the same datasets with corresponding color designations.

Discussion

Direct imaging of HIV virions can provide an important context for understanding how cognate immune responses impact viral replication in vitro and in vivo. Accordingly, both confocal and superresolution microscopy methods have been used to study viral envelope proteins during cell–cell and virus–cell HIV spread (29, 40, 43, 50, 51). Here, we used 3D dSTORM superresoluton techniques to elucidate patterns of conserved, transition state gp120 epitope exposures on individual virions after attachment to $CD4^+$ target cells.

Depending on conditions, it is theoretically possible that each target antigen visualized by dSTORM can be localized more than once due to the binding of multiple antibodies per target, conjugation of multiple dyes per antibody, and/or the stochastic nature of the fluorescence switching process, which leads to even single dye molecules being localized repeatedly. Furthermore, due to the differences in dye properties, the number of blinking cycles varies across different fluorophores; for example, Alexa 488 undergoes fewer blinking cycles than Alexa 647 and Alexa 546.

Recognizing these caveats, the experimental approach used here was configured to examine separate gp120 epitopes with respect to their expression and spatial disposition on a virion. It did not seek to quantify and compare the absolute numbers of different proteins recognized by different antibodies labeled with different dyes. ICAM-1, Vpr, and CD4 signals were used for selecting ROIs and/or to provide orientation markers. All anti-gp120 antibodies were IgG1, labeled with the same dye in the same manner (*SI Methods*). Viral type was the variable in epitope-based comparisons, each type stained with the same antibody. Importantly, because both overcounting or undercounting problems occur randomly, they would have no tendency to generate a systematic spatial bias in relative distributions of the different labeled proteins. The number of localizations analyzed in our experiments was generally less than the expected number of dye molecules per virion in part due to the stringent criteria for accepting a localization into the analyzed dataset. Thus, counting issues should have little impact on the experimental outcomes and interpretations of this particular study.

A previously unsuspected facet of early HIV replication is revealed by observations that conserved CD4i gp120 epitopes become exposed across the surface of an attached virion. The distribution patterns are similar to what occurs with a constitutively expressed, neutralizing gp120 epitope, 2G12. Two lines of evidence suggest that the CD4i exposure patterns extend to virions engaged in active viral replication. First, they occur most extensively on WT virions compared with those that cannot mature or have truncated gp41 C termini (Figs. 5 and 6 and Figs. S3 and S4). Second, dynamic CD4i epitope exposure patterns were selectively observed on bound virion populations experiencing coreceptor-dependent, fusion-permissive content loss (43).

A more unexpected finding is that epitope immunoreactivity was not necessarily adjacent (i.e., within 50 nm) to a CD4 contact. The color-scoring method divided a roughly spherical virion with dimensions up to ∼200 nm in diameter, ∼628-nm circumference, and ∼126 μm^2 in surface area into octants of equal size (Fig. 3*B*). According to this geometry, envelope trimers extant in the green and/or "blue" octants are unlikely to be in contact with CD4. Importantly, these trends were evident in the overall bound

virion population when considered in aggregate. The mAb–CD4 signal angles for CD4i epitopes frequently exceeded 50° (Figs. 4*D* and 6*B* and Fig. S2*C*), although angles were generally larger in virion subsets with one to two potential CD4 contact octants, and smaller in virus groups including more numerous CD4 contact zones (Figs. S1*E* and S2*C* vs. Fig. 4*D*). Such differences were expected as the potential intermolecular distances between envelope and CD4 contact must decrease as either entity is crowded onto the virion surface.

One possible explanation for the above CD4i exposure patterns is suggested by evidence that HIV virions contain allosteric networks, formed by mature envelope–matrix connections (32–35, 37, 41, 42), which can guide the function and position of envelope trimers on the virion surface (12, 40). Given this framework, it is reasonable to posit that receptor-mediated changes in one envelope spike might transmit allosterically to a second, distal structure in the mature virion. This model predicts that the absence of maturation and/or gp41–matrix connections interrupts the network, dampens the transmission of conformational changes around the virion, reduces overall CD4i epitope exposures, and/or decreases the distances from CD4 contact where such antigenic changes occur (e.g., producing smaller epitope–CD4 signal angles). The altered presentation of A32 and C11 epitopes on Y132I and ΔCT mutants vs. WT viruses followed such predictions (Figs. 5 and 6 and Figs. S3 and S4). In cases where the putative allosteric network is disrupted, it is further expected that the impact on epitope exposure should be inversely proportional to the number of potential CD4 contacts over the virion surface (i.e., when allosteric changes traverse only short distances). In accordance, the analyses of mutant viruses reflected that whole populations and/or the subsets with three or more CD4 contact octants exposed A32 and C11 epitopes more extensively than subsets with one to two CD4 contact octants (for example, Fig. S3 vs. Fig. 5). A caveat here is that the mutations we made did not abolish epitope exposure throughout the virion population. Thus, other features of the virion structure may be involved in attachment-based modulation of antigenicity. Furthermore, the virion maturation state had only meager impact on exposure of the 17b CD4i epitope. The 17b epitope is located in the coreceptor binding site (52); the A32 and C11 epitopes are located proximal to gp41 within the envelope trimer (5, 19, 53, 54). A32 and C11 epitope exposure demands relatively extensive structural alterations in the trimer (29, 51, 53), while the coreceptor binding site is amenable to spontaneous exposure, depending on the envelope strain (55). Thus, various CD4i epitopes may arise on bound virions by overlapping mechanisms of protein perturbation.

A second possibility is that bound virions "rock" and/or "roll" over multiple CD4 contacts at the host cell surface, thus experiencing a variety of abortive envelope–receptor binding events before settling on a final prefusion orientation. Each event could leave behind a "trail" of irreversible CD4i conformational perturbations in gp120. In this case, maturation may be an important determinant for such imprinting. Advanced techniques such as live-cell, 3D superresolution imaging might help address this question. It must be considered whether the CD4i epitope signals emanated from putative "shed" gp120 that somehow rebinds to the virion surface. This possibility seems less unlikely as conjugated polyclonal antibody D7324, which marks the presence of free gp120, fails to produce binding signals with the virions and systems used here (43).

HIV envelope spikes have been characterized as partially dispersed or tightly clustered on replication-competent virions, depending on the study (12, 13, 40, 56, 57). Two-dimensional superresolution imaging of HIV by stimulated emission depletion (STED) microscopy indicated that gag maturation may distribute envelope spikes into one or two clusters on the free virion surface (40). Our examination of free virions (Fig. S1*C*) is not necessarily in disagreement with these findings, as we detected envelope trimers mainly within one to four virion octants, most frequently in two adjacent octants (not shown). Sufficiently large patches of envelope spikes could overlap adjacent octants depending on their orientation vs. the virion sectioning. STED imaging also indicated that envelope trimers on attached virions remained clustered toward the cell surface. Cryo-EM ensemble imaging indicated a similar arrangement of surface structures toward cell contacts (12). However, the virions in these studies appeared to be situated near a single CD4 contact point, which was a rare instance in the ROIs examined here (Fig. S1*B*). In particular, a tightly localized cluster of CD4 might deliver avidity effects that maintains a congregation of envelope spikes. In cases where multiple CD4 contacts occur (the more frequent likelihood on TZM-bl cells), any single receptor molecule may not favor another in terms of attracting surface envelope trimers, thus creating a more dispersed distribution pattern of structurally altered gp120. Another noteworthy difference between a previous report (40) and the current study is that the former used STED, which produces 2D imaging, whereas the latter used a 3D imaging approach, offering a wider perspective.

Antibodies are equipped to disrupt viral replication by Fab-mediated chemical interference in viral function (i.e., direct neutralization) and/or by Fc binding to an array of FcRs on effector cells, which can abrogate nascent infection by a variety of mechanisms (e.g., ADCC). These two modes of action can be separable because Fc-dependent mechanisms require only that an antibody mark the presence of a virion fast enough to allow recruited effector cells to interrupt the replication process. Our findings for single virions provide insight into how and why CD4i epitopes might unreliably initiate direct neutralizing effects yet succeed in mediating other humoral antiviral effector functions. First, antibodies recognizing CD4i epitope presentation distal to fusogenic contact zones are almost certainly not neutralizing as they have little or no opportunity to directly interfere with active replication mechanisms. Second, immunoreactive CD4i epitopes presented closer to potential CD4 contacts could mark "off-pathway," nonfusogenic attachment structures. The existence of such structures was suggested by previous demonstrations that mAbs against transition state gp41 domains failed to block cell–cell HIV fusion even though the epitopes appeared within intercellular contact zones (51). Third, certain CD4i epitopes, such as A32 and C11, might arise on fusogenic envelope spikes, but only after the gp41 fusion machinery has been irreversibly triggered to allow content delivery. Structural data for such epitopes indicate that this scenario is possible, if not likely (53).

Overall, the imaging data indicate that transition state structures and their CD4i epitopes arise on mature, cell-bound virions shortly after attachment. Such epitope exposure patterns clearly have the potential to engage cognate antibodies in a manner capable of recruiting humoral effector cells to achieve an FcR-dependent antiviral effect. In accordance, it has been shown that anti-CD4i epitope antibodies mediate FcR-dependent effector mechanisms against bound virions in vitro (20, 58). From the standpoint of translational efforts, Ig domain-based agents targeting the A32 epitope have already shown promise in suppressing HIV infection (30, 31). Transition state gp120 antigens trials (59, 60) expressing A32 and other conserved CD4i epitopes have been used to generate protective anti-HIV envelope humoral responses in nonhuman primate models of infection (25, 26) and are now being tested in early-phase clinical trials. Direct imaging of transition state structures and epitopes on attached HIV virions should inform the interpretation and expansion of these and related efforts. Additional insights for managing HIV replication with anti-envelope antibody responses should arise from continued efforts to directly interrogate the antigenic nature of HIV during early replication.

Methods

See *Supporting Information* for detailed methods.

HIV_{JRFL} pseudoviruses (CCR5-tropic; tier 2 neutralization sensitivity) expressing SNAP–ICAM-1 and CLIP–Vpr were generated as previously described (43) using HEK 293T cells. WT as well as two mutant variants, one with a matrix/capsid processing site mutation (Y132I), and a second with Env truncated at residue 708 (ΔCT), were generated by cotransfection as described in *Supporting Information*. Pseudoviruses were fluorescently labeled via SNAP–ICAM-1 or CLIP–Vpr with SNAP–Surface Alexa 546 and CLIP–Cell Alexa 360, respectively.

TZM-bl cells expressing CD4 and CCR5 were seeded on glass-bottom dishes overnight, then cocultured with 0.5 mL (700 ng/mL gp120 equivalents) of fluorescently labeled virions along with 5 μg/mL Alexa 647-conjugated anti-CD4 mAb OKT4 for 30 min at 37 °C. Cocultures were then immediately fixed with 4% paraformaldehyde for 10 min at room temperature. Nonspecific interactions were blocked by incubating the dishes with 10% normal goat serum containing 100 μg/mL nonspecific human IgG1 solution for 30 min at room temperature. Epitopes of interest were then probed with Alexa 488-conjugated antibodies 2G12, A32, C11, and 17b, using an incubation period of 30 min at room temperature. Synagis served as a nonspecific negative control used under identical conditions. Dishes were then postfixed in 4% paraformaldehyde for 10 min at room temperature and stored in 1× PBS at 4 °C until imaging.

For image acquisition, PBS storage buffer was replaced with an oxygen-scavenging imaging buffer (*Supporting Information*). These dishes were then placed on a Nikon N-STORM microscope to obtain three-color, 3D dSTORM images. The 647-, 561-, and 488-nm laser lines were used to excite Alexa 647-conjugated OKT4, SNAP–ICAM-1 labeled with SNAP–Surface Alexa 546, and Alexa 488-conjugated mAbs, respectively. The 405 laser was used to locate virus particles on TZM-bl cell surfaces via TIRF imaging of CLIP–Vpr Alexa 360 signals. A cylindrical lens was used for astigmatic 3D-STORM imaging (46). Single-molecule fitting of the centroid position and the widths in the *x* and *y* direction, as well as the *z* position of molecules, and Gaussian images were rendered using the Nikon NIS-Elements AR software. Drift correction was performed to identify the positions of all three fluorophores, and their localization precision was determined to be 20 nm (Alexa 647) and 30 nm (Alexa 488 and 546) using full width at half-maximum (FWHM), with a 50-nm axial resolution. After high-resolution images were obtained, ROIs were defined around single virions with SNAP–ICAM-1 and Vpr signals colocated within a 200-nm space (density filter: radius, ≤100) proximal (within 50 nm; see below) of an anti-CD4 antibody signal. Snap shots of Gaussian signal images were taken at four 90° views for each ROI.

The localized molecules and their positions were recorded in these ROIs and exported as text files for further analysis with MATLAB software. The 3D SNAP–ICAM-1 and test mAb localizations were used as coordinates to fit a sphere with a diameter less than 200 nm (least-square method, with the radius limited in the 50- to 100-nm range). To do this, a custom code [MATLAB File Exchange (title: HIV Sphere Fit and Angle Calculation; file ID 57198)] was developed (*Supporting Information*). Proximal CD4 localizations (via anti-CD4 antibody) were also imported to determine their relative positions to mAb signals.

Spheres generated as described above were used to determine anti-gp120 mAb binding locations relative to cell surface CD4. SNAP–ICAM-1, test mAb, and CD4 (mAb OKT4) localized signals were situated relative to the fitted sphere in each ROI. CD4 localizations within 50 nm of fitted spheres were considered as possible contact points. Two approaches were used to determine mAb positions relative to CD4: (*i*) Octant color scoring: Fitted spheres delineating virions were divided into eight equally sized segments (octants) to position localized antibody signals relative to anti-CD4 antibody signals (see schematic in Fig. 3*B*). Octants containing fluorescent mAb signals were color scored according to their distance from the nearest potential CD4 contact zone, marked by anti-CD4 OKT4 signals (herein designated a CD4 contact octant): (*a*) CD4 contact octant and antibody signals within the same octant, yellow; (*b*) CD4 contact octant vs. antibody signal octants with sides in contact, green; (*c*) CD4 contact octant vs. antibody signal octants with tips in contact, cyan; (*d*) CD4 contact octant vs. antibody signal octants with no contacts, pink. Categorical comparisons of these color-coding schemes for different experimental conditions were performed using multicategory Fisher exact tests (see below for description). (*ii*) Angle analysis: The MATLAB code described above includes a function to extract spherical angles between every test mAb fluorescence signal vs. its nearest anti-CD4 OKT4 signal, illustrated as shown in Fig. 3*C*. As noted above, anti-CD4 (mAb OKT4), SNAP–ICAM-1, or anti-gp120 (test mAb) fluorescence signals were used to fit centroids (NIS Elements N-STORM software) marking the positions of CD4, SNAP–ICAM-1, or gp120 epitopes, respectively. Only CD4 molecular signals located ≤50 nm from the calculated virion surface were taken as potential virus–receptor contacts and used to generate measures. Using the MATLAB code, spherical angles between the calculated positions of each epitope and its nearest putative CD4 contact were determined using the center of the virion "sphere" as the vertex for the corresponding rays. Note that this method accommodates the fact that an octant designated as a contact octant can comprise multiple CD4 positions that are ≤50 nm from the virion surface and that an ROI may harbor multiple epitope exposure sites. Thus, the total measures for angle analyses are greater than the number of ROIs examined for any given epitope.

As a comparative control, octant color-scoring and angle analyses were similarly carried out with SNAP–ICAM-1 localizations instead of test mAbs. Statistical differences in antibody distributions between the various experimental conditions were evaluated using Wilcoxon–Mann–Whitney *U* tests (see *Supporting Information* for statistical analyses).

ACKNOWLEDGMENTS. This work was supported by Bill and Melinda Gates Foundation Grants OPP1033109 (to G.K.L.) and OPP1017606 and OPP41351 (to R.C.G.), and in part by the Intramural Research Program of the NIH, National Library of Medicine (M.W.G. and J.L.S.).

1. Lewis GK, Pazgier M, DeVico AL (2017) Survivors remorse: Antibody-mediated protection against HIV-1. *Immunol Rev* 275:271–284.
2. Klasse PJ (2012) The molecular basis of HIV entry. *Cell Microbiol* 14:1183–1192.
3. Wilen CB, Tilton JC, Doms RW (2012) Molecular mechanisms of HIV entry. *Adv Exp Med Biol* 726:223–242.
4. DeVico AL (2007) CD4-induced epitopes in the HIV envelope glycoprotein, gp120. *Curr HIV Res* 5:561–571.
5. Lewis GK, et al. (2014) Epitope target structures of Fc-mediated effector function during HIV-1 acquisition. *Curr Opin HIV AIDS* 9:263–270.
6. Gonzalez MW, DeVico AL, Lewis GK, Spouge JL (2015) Conserved molecular signatures in gp120 are associated with the genetic bottleneck during simian immunodeficiency virus (SIV), SIV-human immunodeficiency virus (SHIV), and HIV type 1 (HIV-1) transmission. *J Virol* 89:3619–3629.
7. Lyumkis D, et al. (2013) Cryo-EM structure of a fully glycosylated soluble cleaved HIV-1 envelope trimer. *Science* 342:1484–1490.
8. Sanders RW, et al. (2013) A next-generation cleaved, soluble HIV-1 Env trimer, BG505 SOSIP.664 gp140, expresses multiple epitopes for broadly neutralizing but not non-neutralizing antibodies. *PLoS Pathog* 9:e1003618.
9. Lee JH, Ozorowski G, Ward AB (2016) Cryo-EM structure of a native, fully glycosylated, cleaved HIV-1 envelope trimer. *Science* 351:1043–1048.
10. Bennett A, et al. (2007) Cryoelectron tomographic analysis of an HIV-neutralizing protein and its complex with native viral gp120. *J Biol Chem* 282:27754–27759.
11. Liu J, Bartesaghi A, Borgnia MJ, Sapiro G, Subramaniam S (2008) Molecular architecture of native HIV-1 gp120 trimers. *Nature* 455:109–113.
12. Sougrat R, et al. (2007) Electron tomography of the contact between T cells and SIV/HIV-1: Implications for viral entry. *PLoS Pathog* 3:e63.
13. Zhu P, et al. (2006) Distribution and three-dimensional structure of AIDS virus envelope spikes. *Nature* 441:847–852.
14. Burton DR, et al. (2004) HIV vaccine design and the neutralizing antibody problem. *Nat Immunol* 5:233–236.
15. Labrijn AF, et al. (2003) Access of antibody molecules to the conserved coreceptor binding site on glycoprotein gp120 is sterically restricted on primary human immunodeficiency virus type 1. *J Virol* 77:10557–10565.
16. Poignard P, Saphire EO, Parren PW, Burton DR (2001) gp120: Biologic aspects of structural features. *Annu Rev Immunol* 19:253–274.
17. Burton DR, Stanfield RL, Wilson IA (2005) Antibody vs. HIV in a clash of evolutionary titans. *Proc Natl Acad Sci USA* 102:14943–14948.
18. Karlsson Hedestam GB, et al. (2008) The challenges of eliciting neutralizing antibodies to HIV-1 and to influenza virus. *Nat Rev Microbiol* 6:143–155.
19. Ray K, et al. (2014) Antigenic properties of the HIV envelope on virions in solution. *J Virol* 88:1795–1808 and correction (2014) 88:5901.
20. Guan Y, et al. (2013) Diverse specificity and effector function among human antibodies to HIV-1 envelope glycoprotein epitopes exposed by CD4 binding. *Proc Natl Acad Sci USA* 110:E69–E78.
21. Pollara J, et al. (2013) Epitope specificity of human immunodeficiency virus-1 antibody dependent cellular cytotoxicity [ADCC] responses. *Curr HIV Res* 11:378–387.
22. Haynes BF, et al. (2012) Immune-correlates analysis of an HIV-1 vaccine efficacy trial. *N Engl J Med* 366:1275–1286.
23. Ferrari G, et al. (2011) An HIV-1 gp120 envelope human monoclonal antibody that recognizes a C1 conformational epitope mediates potent ADCC activity and defines a common ADCC epitope in human HIV-1 serum. *J Virol* 85:7029–7036.
24. Tomaras GD, et al. (2013) Vaccine-induced plasma IgA specific for the C1 region of the HIV-1 envelope blocks binding and effector function of IgG. *Proc Natl Acad Sci USA* 110:9019–9024.
25. Fouts TR, et al. (2015) Balance of cellular and humoral immunity determines the level of protection by HIV vaccines in rhesus macaque models of HIV infection. *Proc Natl Acad Sci USA* 112:E992–E999.

26. DeVico A, et al. (2007) Antibodies to CD4-induced sites in HIV gp120 correlate with the control of SHIV challenge in macaques vaccinated with subunit immunogens. *Proc Natl Acad Sci USA* 104:17477–17482.
27. Mabuka J, Nduati R, Odem-Davis K, Peterson D, Overbaugh J (2012) HIV-specific antibodies capable of ADCC are common in breastmilk and are associated with reduced risk of transmission in women with high viral loads. *PLoS Pathog* 8:e1002739.
28. Milligan C, Richardson BA, John-Stewart G, Nduati R, Overbaugh J (2015) Passively acquired antibody-dependent cellular cytotoxicity (ADCC) activity in HIV-infected infants is associated with reduced mortality. *Cell Host Microbe* 17:500–506.
29. Finnegan CM, Berg W, Lewis GK, DeVico AL (2001) Antigenic properties of the human immunodeficiency virus envelope during cell-cell fusion. *J Virol* 75:11096–11105.
30. Sung JA, et al. (2015) Dual-affinity re-targeting proteins direct T cell-mediated cytolysis of latently HIV-infected cells. *J Clin Invest* 125:4077–4090.
31. Sloan DD, et al. (2015) Targeting HIV reservoir in infected CD4 T cells by dual-affinity re-targeting molecules (DARTs) that bind HIV envelope and recruit cytotoxic T cells. *PLoS Pathog* 11:e1005233.
32. Davis MR, Jiang J, Zhou J, Freed EO, Aiken C (2006) A mutation in the human immunodeficiency virus type 1 Gag protein destabilizes the interaction of the envelope protein subunits gp120 and gp41. *J Virol* 80:2405–2417.
33. Wyma DJ, Kotov A, Aiken C (2000) Evidence for a stable interaction of gp41 with Pr55 (Gag) in immature human immunodeficiency virus type 1 particles. *J Virol* 74: 9381–9387.
34. Murakami T, Ablan S, Freed EO, Tanaka Y (2004) Regulation of human immunodeficiency virus type 1 Env-mediated membrane fusion by viral protease activity. *J Virol* 78:1026–1031.
35. Wyma DJ, et al. (2004) Coupling of human immunodeficiency virus type 1 fusion to virion maturation: A novel role of the gp41 cytoplasmic tail. *J Virol* 78:3429–3435.
36. Joyner AS, Willis JR, Crowe JE, Jr, Aiken C (2011) Maturation-induced cloaking of neutralization epitopes on HIV-1 particles. *PLoS Pathog* 7:e1002234.
37. Tedbury PR, Ablan SD, Freed EO (2013) Global rescue of defects in HIV-1 envelope glycoprotein incorporation: Implications for matrix structure. *PLoS Pathog* 9: e1003739.
38. Bhatia AK, Campbell N, Panganiban A, Ratner L (2007) Characterization of replication defects induced by mutations in the basic domain and C-terminus of HIV-1 matrix. *Virology* 369:47–54.
39. Murakami T, Freed EO (2000) Genetic evidence for an interaction between human immunodeficiency virus type 1 matrix and alpha-helix 2 of the gp41 cytoplasmic tail. *J Virol* 74:3548–3554.
40. Chojnacki J, et al. (2012) Maturation-dependent HIV-1 surface protein redistribution revealed by fluorescence nanoscopy. *Science* 338:524–528.
41. Alfadhli A, Barklis RL, Barklis E (2009) HIV-1 matrix organizes as a hexamer of trimers on membranes containing phosphatidylinositol-(4,5)-bisphosphate. *Virology* 387: 466–472.
42. Frank GA, et al. (2015) Maturation of the HIV-1 core by a non-diffusional phase transition. *Nat Commun* 6:5854.
43. Mengistu M, Ray K, Lewis GK, DeVico AL (2015) Antigenic properties of the human immunodeficiency virus envelope glycoprotein gp120 on virions bound to target cells. *PLoS Pathog* 11:e1004772.
44. Wei X, et al. (2003) Antibody neutralization and escape by HIV-1. *Nature* 422: 307–312.
45. Briggs JA, Wilk T, Welker R, Kräusslich HG, Fuller SD (2003) Structural organization of authentic, mature HIV-1 virions and cores. *EMBO J* 22:1707–1715.
46. Huang B, Wang W, Bates M, Zhuang X (2008) Three-dimensional super-resolution imaging by stochastic optical reconstruction microscopy. *Science* 319:810–813.
47. Trkola A, et al. (1995) Cross-clade neutralization of primary isolates of human immunodeficiency virus type 1 by human monoclonal antibodies and tetrameric CD4-IgG. *J Virol* 69:6609–6617.
48. Lee SK, Harris J, Swanstrom R (2009) A strongly transdominant mutation in the human immunodeficiency virus type 1 gag gene defines an Achilles heel in the virus life cycle. *J Virol* 83:8536–8543.
49. Binley JM, et al. (2003) Redox-triggered infection by disulfide-shackled human immunodeficiency virus type 1 pseudovirions. *J Virol* 77:5678–5684.
50. Dirk BS, Van Nynatten LR, Dikeakos JD (2016) Where in the cell are you? Probing HIV-1 host interactions through advanced imaging techniques. *Viruses* 8:E288.
51. Finnegan CM, Berg W, Lewis GK, DeVico AL (2002) Antigenic properties of the human immunodeficiency virus transmembrane glycoprotein during cell-cell fusion. *J Virol* 76:12123–12134.
52. Xiang SH, Doka N, Choudhary RK, Sodroski J, Robinson JE (2002) Characterization of CD4-induced epitopes on the HIV type 1 gp120 envelope glycoprotein recognized by neutralizing human monoclonal antibodies. *AIDS Res Hum Retroviruses* 18: 1207–1217.
53. Acharya P, et al. (2014) Structural definition of an antibody-dependent cellular cytotoxicity response implicated in reduced risk for HIV-1 infection. *J Virol* 88: 12895–12906.
54. Gohain N, et al. (2015) Co-crystal structures of antibody N60-i3 and antibody JR4 in complex with gp120 define more cluster A epitopes involved in effective antibody-dependent effector function against HIV-1. *J Virol* 89:8840–8854.
55. Sullivan N, et al. (1998) CD4-induced conformational changes in the human immunodeficiency virus type 1 gp120 glycoprotein: Consequences for virus entry and neutralization. *J Virol* 72:4694–4703.
56. Galimidi RP, et al. (2015) Intra-spike crosslinking overcomes antibody evasion by HIV-1. *Cell* 160:433–446.
57. Mouquet H, et al. (2010) Polyreactivity increases the apparent affinity of anti-HIV antibodies by heteroligation. *Nature* 467:591–595.
58. Lewis GK (2014) Role of Fc-mediated antibody function in protective immunity against HIV-1. *Immunology* 142:46–57.
59. Fouts TR, et al. (2000) Expression and characterization of a single-chain polypeptide analogue of the human immunodeficiency virus type 1 gp120-CD4 receptor complex. *J Virol* 74:11427–11436.
60. Schwartz JA, et al. (2016) An HIV gp120-CD4 immunogen does not elicit autoimmune antibody responses in cynomolgus macaques. *Clin Vaccine Immunol* 23:618–627.
61. Platt EJ, Bilska M, Kozak SL, Kabat D, Montefiori DC (2009) Evidence that ecotropic murine leukemia virus contamination in TZM-bl cells does not affect the outcome of neutralizing antibody assays with human immunodeficiency virus type 1. *J Virol* 83: 8289–8292.
62. Takeuchi Y, McClure MO, Pizzato M (2008) Identification of γ-retroviruses constitutively released from cell lines used for HIV research. *J Virol* 82:12585–12588.
63. Wei X, et al. (2002) Emergence of resistant human immunodeficiency virus type 1 in patients receiving fusion inhibitor (T-20) monotherapy. *Antimicrob Agents Chemother* 46: 1896–1905.
64. Derdeyn CA, et al. (2000) Sensitivity of human immunodeficiency virus type 1 to the fusion inhibitor T-20 is modulated by coreceptor specificity defined by the V3 loop of gp120. *J Virol* 74:8358–8367.
65. Platt EJ, Wehrly K, Kuhmann SE, Chesebro B, Kabat D (1998) Effects of CCR5 and CD4 cell surface concentrations on infections by macrophagetropic isolates of human immunodeficiency virus type 1. *J Virol* 72:2855–2864.
66. Wei X, et al. (2002) Emergence of resistant human immunodeficiency virus type 1 in patients receiving fusion inhibitor (T-20) monotherapy. *Antimicrob Agents Chemother* 46: 1896–1905.
67. Li M, et al. (2006) Genetic and neutralization properties of subtype C human immunodeficiency virus type 1 molecular env clones from acute and early heterosexually acquired infections in Southern Africa. *J Virol* 80:11776–11790.
68. van de Linde S, et al. (2011) Direct stochastic optical reconstruction microscopy with standard fluorescent probes. *Nat Protoc* 6:991–1009.
69. Dudok B, et al. (2015) Cell-specific STORM super-resolution imaging reveals nanoscale organization of cannabinoid signaling. *Nat Neurosci* 18:75–86.
70. Dani A, Huang B, Bergan J, Dulac C, Zhuang X (2010) Superresolution imaging of chemical synapses in the brain. *Neuron* 68:843–856.
71. Laplante C, Huang F, Tebbs IR, Bewersdorf J, Pollard TD (2016) Molecular organization of cytokinesis nodes and contractile rings by super-resolution fluorescence microscopy of live fission yeast. *Proc Natl Acad Sci USA* 113:E5876–E5885.
72. Benjamini Y, Cohen R (2017) Weighted false discovery rate controlling procedures for clinical trials. *Biostatistics* 18:91–104.
73. Reiner A, Yekutieli D, Benjamini Y (2003) Identifying differentially expressed genes using false discovery rate controlling procedures. *Bioinformatics* 19:368–375.
74. Siegel S, Castellan NJ (1988) *Nonparametric Statistics for the Behavioral Sciences* (McGraw-Hill, New York), 2nd Ed.
75. Fisher RA (1970) *Statistical Methods for Research Workers* (Hafner Publishing Company, New York), 14th Ed.